

Article

Enhanced Photocatalytic Activity of Spherical Nd³⁺ Substituted ZnFe₂O₄ Nanoparticles

Loan T. T. Nguyen ^{1,*}, Hang T. T. Nguyen ², Thieng H. Le ¹, Lan T. H. Nguyen ¹, Hai Q. Nguyen ¹, Thanh T. H. Pham ¹, Nguyen D. Bui ¹, Ngan T. K. Tran ^{3,4}, Duyen Thi Cam Nguyen ^{3,4}, Tan Van Lam ^{3,4,*} and Thuan Van Tran ^{3,4,*}

- ¹ Faculty of Chemistry, Thai Nguyen University of Education, Thai Nguyen 24000, Vietnam; lehuuthieng@dhsptn.edu.vn (T.H.L.); lannth.chem@tnue.edu.vn (L.T.H.N.); hainq@tnue.edu.vn (H.Q.N.); thanhpth@tnue.edu.vn (T.T.H.P.); ducnguyen@tnue.edu.vn (N.D.B.)
- ² Faculty of Fundamental Sciences, Thai Nguyen University of Technology, Thai Nguyen 24000, Vietnam; thuyhangtnut@gmail.com
- ³ NTT Hi-Tech Institute, Nguyen Tat Thanh University, Ho Chi Minh 700000, Vietnam; ttkngan@ntt.edu.vn (N.T.K.T.); ntcduyen@ntt.edu.vn (D.T.C.N.)
- ⁴ Center of Excellence for Green Energy and Environmental Nanomaterials, Nguyen Tat Thanh University, Ho Chi Minh 700000, Vietnam
- * Correspondence: loanntt@tnue.edu.vn (L.T.T.N.); lvtan@ntt.edu.vn (T.V.L.); tranvt@ntt.edu.vn (T.V.T.)

Abstract: In this study, nanocrystalline ZnNd_xFe_{2-x}O₄ ferrites with x = 0.0, 0.01, 0.03 and 0.05 were fabricated and used as a catalyst for dye removal potential. The effect of Nd³⁺ ions substitution on the structural, optical and photo-Fenton activity of ZnNd_xFe_{2-x}O₄ has been investigated. The addition of Nd³⁺ ions caused a decrease in the grain size of ferrites, the reduction of the optical bandgap energies and thus could be well exploited for the catalytic study. The photocatalytic activity of the ferrite samples was evaluated by the degradation of Rhodamine B (RhB) in the presence of H₂O₂ under visible light radiation. The results indicated that the ZnNd_xFe_{2-x}O₄ samples exhibited higher removal efficiencies than the pure ZnFe₂O₄ ferrites. The highest degradation efficiency was 98.00%, attained after 210 min using the ZnNd_{0.03}Fe_{1.97}O₄ sample. The enhanced photocatalytic activity of the ZnFe₂O₄ doped with Nd³⁺ is explained due to the efficient separation mechanism of photoinduced electron and holes. The effect of various factors (H₂O₂ oxidant concentration and catalyst loading) on the degradation of RhB dye was clarified.

Keywords: zinc ferrite; neodymium-doping; photo-Fenton; Rhodamine B



Citation: Nguyen, L.T.T.; Nguyen, H.T.T.; Le, T.H.; Nguyen, L.T.H.; Nguyen, H.Q.; Pham, T.T.H.; Bui, N.D.; Tran, N.T.K.; Nguyen, D.T.C.; Lam, T.V.; et al. Enhanced Photocatalytic Activity of Spherical Nd³⁺ Substituted ZnFe₂O₄ Nanoparticles. *Materials* **2021**, *14*, 2054. <https://doi.org/10.3390/ma14082054>

Academic Editor: Luminița Isac

Received: 4 March 2021

Accepted: 16 April 2021

Published: 19 April 2021

Publisher's Note: MDPI stays neutral with regard to jurisdictional claims in published maps and institutional affiliations.



Copyright: © 2021 by the authors. Licensee MDPI, Basel, Switzerland. This article is an open access article distributed under the terms and conditions of the Creative Commons Attribution (CC BY) license (<https://creativecommons.org/licenses/by/4.0/>).

1. Introduction

It has been proved that the discharge of organic compounds, including dyes, from manufacturing plants led to growing contamination in the aquatic ecosystem [1,2]. There are numerous impacts of color pollution, so more and more techniques have been found to address this environmental problem [3]. Among them, photocatalysis, which relies on semiconductors and irradiation-based degradation of organic substances, is an effective method [4,5]. The benefits of this approach include environmental friendliness, the potential to entirely decompose organic pollutants into inorganic molecules, i.e., CO₂ and H₂O. TiO₂ [6–8], WO₃ [9–13], and BiVO₄ [14,15] are typical photocatalysts that have been well studied for dyes degradation. Nano ferrites, another material, have recently received a great deal of interest due to their high stability, strong magnetic properties, and high catalytic performance. In particular, such nanoparticles may be used as a photocatalyst under visible light in wastewater treatment thanks to their narrow band gap [16,17]. In addition, the method used for ferrite synthesis may differ depending on the desired characteristics, and a number of synthesis routes have been investigated so far, like solvothermal [18], sol-gel [19], coprecipitation [20], and combustion method [21]. For example, Xiaojun Guo et al. [17] reported that the NiFe₂O₄ hollow nanospheres synthesized by solvothermal method had

a high photoactivity for methylene blue (MB) degradation, which achieved the removal efficiency of approximately 98.5% only within 50 min in the presence of 5 mM H_2O_2 and $0.06 \text{ g}\cdot\text{L}^{-1}$ $\text{H}_2\text{C}_2\text{O}_4$. In other extensive studies on ferrite, ZnFe_2O_4 nanomaterial has been documented to be effective in removing a wide range of organic compounds, such as Orange II [22], Red 88, Acid Orange 8, Malachite Green [23], Congo red [24], methylene blue [25] and tetracycline [26]. Besides, MnFe_2O_4 , CoFe_2O_4 , CuFe_2O_4 and MgFe_2O_4 nanospinels have been reported to show effective photocatalytic activity to eliminate distinct categories of dyes [19,20,27,28]. Because of the fact that ferrite catalysts can be easily recoverable using an external magnetic field, these promising potentials have rendered any successful effort to improve their photocatalytic efficiency in substantiating their practical system uses [29].

It was previously noted that the structural features and magnetic, electrical characteristics and catalytic activity of ferrites could be dependent on the metals in the ferrite lattice structure [30]. In addition, several studies have reported the enhancement in the catalytic activity of ferrites with different metal substitution and change in cation distribution. For instance, the photocatalytic activity of cobalt zinc ferrite systems on Mn substitution has been documented by Santosh Bhukal et al. [31], showing that the decolorization ratio of methyl orange is enhanced along with increasing Mn^{3+} ions content. In another study, MgFe_2O_4 doped with Co^{2+} ions by modified sol-gel combustion method exhibited higher degradation efficiency for methylene blue in comparison with that of pure MgFe_2O_4 sample [32]. Similar results were obtained with nickel ferrite when substituted with Zn [33].

On the other hand, the substitution that gained attention in doping ferrite iron was rare-earth ions [34–38]. Since these metals have a strong spin-orbit coupling of angular momentum due to the presence of unpaired electrons in the 4f orbitals, their interaction with ferrites occurs in 3d-4f coupling, resulting in magneto-crystalline anisotropy and thus influencing magnetic, electrical and catalytic features of substituted ferrites [39]. Mariosi et al. found that cobalt ferrite nanoparticles substituted by La^{3+} ions exhibited structural changes in terms of cationic arrangement of the spinel structure [38]. This change resulted in a decrease in coercivity values and an increase in the surface area. The substitution of other rare-earth ions such as La^{3+} , Nd^{3+} , Gd^{3+} and Dy^{3+} into the [B] sites containing iron has been shown to displace Fe^{3+} into (A) sites, thus altering the structure and electrical and magnetic characteristics the ferrites [34,35,37,39]. Sharma et al. have carried out one prominent study showing the ability of rare-earth doping to boost catalytic activity [40]. Specifically, rare-earth (La^{3+} , Ce^{3+}) substituted CoFe_2O_4 exhibited higher efficiencies in the elimination of five model pollutants, possibly due to the presence of $\text{Ce}^{3+}/\text{Ce}^{4+}$ redox pair. The synthesis of samarium (Sm^{3+}) substituted manganese ferrite nanoparticles ($\text{MnFe}_{2-x}\text{Sm}_x\text{O}_4$) using oleic acid as a surfactant was reported by Rashmi et al. [41]. Such synthesized nanomaterials were tested for photocatalytic degradation of colors under visible light irradiation. Such synthesized nanomaterials were tested for photocatalytic degradation of colors under visible light irradiation. The result indicated that samarium replacement significantly increased the photocatalytic activity of MnFe_2O_4 nanoparticles. The value of x varied from 0, 0.5, 1.0, 1.5 and 2.0, and the best results were obtained at $x = 1.5$. The higher activity of $x = 1.5$ was related to its minimum band gap energy value (1.64 eV). After that, Patil et al. [42] synthesized Gd^{3+} doped ZnFe_2O_4 ($\text{ZnFe}_{2-x}\text{Gd}_x\text{O}_4$) nanoparticles via coprecipitation method. Synthesized photocatalysts were checked for MB photo-degradation, resulting in enhanced degradation of MB, from about 95 to 99% in the presence of photocatalysts $\text{ZnFe}_{2-x}\text{Gd}_x\text{O}_4$ ($x = 0, 0.3, 0.5$ and 0.7) along with 8 ppm of H_2O_2 . The efficiency level was found higher than that of the pristine ZnFe_2O_4 and could be attributable to the fact that Fermi energy levels of substituted catalyst were just below the conduction band within the energy band gap. In addition, formation of lattice strains due to the difference between ionic radii of Gd^{3+} (0.94 Å) and that of Fe^{3+} (0.78 Å) is also partially responsible for the enhancement. However, the impact of rare earth substitution (e.g., Nd) on the photo-Fenton activity of ferrites for dye degradation is still a gap in the literature.

The present study aims to investigate the structural and catalytic properties of ferrites by the doping substitution of Nd^{3+} ions. ZnFe_2O_4 was incorporated with various Nd^{3+} molar ratio (0–0.05 mol%) using urea as a fuel additive. The as-synthesized ferrite was then characterized using several techniques (XRD, SEM, TEM, EDX, and FT-IR) before being tested for photocatalytic activities toward Rhodamine B. The effect of catalyst loading, H_2O_2 concentration, and contact time on the photo catalytic activity of ZnFe_2O_4 nanoparticles was surveyed meticulously.

2. Materials and Methods

2.1. Synthesis of $\text{ZnNd}_x\text{Fe}_{2-x}\text{O}_4$ Nanoparticles

Firstly, urea coprecipitation method was adopted to fabricate nanocrystalline $\text{ZnNd}_x\text{Fe}_{2-x}\text{O}_4$ ($x = 0, 0.01, 0.03, 0.05$) ferrites according to a previous publication with a moderate modification [34]. Analytical grade zinc nitrate tetrahydrate [$\text{Zn}(\text{NO}_3)_2 \cdot 4\text{H}_2\text{O}$, 98% pure, Sigma-Aldrich, Darmstadt, Germany], iron(II) nitrate nonahydrate [$\text{Fe}(\text{NO}_3)_3 \cdot 9\text{H}_2\text{O}$, 99.9% pure, Sigma-Aldrich], and neodymium(III) nitrate hexahydrate ($\text{Nd}(\text{NO}_3)_3 \cdot 6\text{H}_2\text{O}$, 99.9% pure, Sigma-Aldrich) were used as oxidizer and urea ($\text{CH}_4\text{N}_2\text{O}$, >99% pure, Sigma-Aldrich) was used as a fuel additive. A number of proper ions: Zn^{2+} (1 mmol) combined with Fe^{3+} [(2– x) mol] and Nd^{3+} (x mol) ($x = 0, 0.01, 0.03, 0.05$) were dissolved in distilled water. The final pH of the solution was adjusted at 5.0, and then was heated to 100 °C for 1 h. The precipitation was collected, washed with distilled water (3×20 mL) to eliminate metal ion and anion traces and then calcinated up to 500 °C for 2 h (ramping rate of 10 °C/min). The product was ground and stored at a vacuum container.

2.2. Characterization

The as-synthesized particles were characterized using a number of techniques including X-ray diffraction (XRD), Fourier-transform infrared spectroscopy (FT-IR), scanning electron microscope (SEM), transmission electron microscopy (TEM), energy dispersive X-ray spectroscopy (EDX) and UV-Vis absorption spectroscopy. Respective instruments for those analyses include D8 Advance diffractometer (Bruker, Madison, WI, USA) with CuK_α radiation ($\lambda = 1.5406 \text{ \AA}$) in a 2θ angle ranging from 20° to 70° with a step of 0.03° source, FTIR Affinity-1S (Shimadzu, Kyoto, Japan), Hitachi S-4800 (Tokyo, Japan), JEOL-JEM-1010 (Tokyo, Japan), JEOL JED 2300 Analysis Station (Tokyo, Japan) and U-4100 (Hitachi, Tokyo, Japan) operating in the wavelength range of 200–800 nm.

2.3. Photocatalytic Degradation of Rhodamine B

In this study, Rhodamine B (RhB) was used as target pollutant to assess the photocatalytic potential of as-synthesized ferrite samples. Accordingly, the RhB degradation reaction was carried out in a reactor containing the $\text{ZnNd}_x\text{Fe}_{2-x}\text{O}_4$ ($x = 0, 0.01, 0.03, 0.05$) nanoparticles and RhB dye under visible light irradiation (using 30 W Led lamps, Philips, Amsterdam, Netherlands). In a typical experiment, 0.1 g of catalyst was introduced into 200 mL of RhB aqueous solution ($10 \text{ mg} \cdot \text{L}^{-1}$) and suspended on a shaker table at 200 rpm. The suspension was first stirred in the dark for 30 min to attain the adsorption-desorption equilibrium state between the catalyst and RhB. Afterwards, the reaction was stirred and H_2O_2 30% (w/w) in H_2O (Sigma-Aldrich) was added to the mixture, which was then irradiated under visible light for 210 min. To determine the RhB concentration in the mixture, 5 mL of each aliquot was taken out periodically, then centrifuged to remove the solid catalyst. The effect of two factors including H_2O_2 concentrations (0.02 M, 0.04 M and 0.06 M) and the catalyst dosages (0.5, 0.75 and 1.0 g/L) on the photo-degradation efficiency was studied.

The efficient degradation of RhB (H) was calculated according to the formula Equation (1).

$$H = \frac{C_0 - C_t}{C_0} \times 100 \quad (1)$$

where C_0 and C_t are the concentration of RhB ($\text{mg}\cdot\text{L}^{-1}$) at the time 0 and t . The samples were measured by scanning at the maximum wavelength $\lambda = 553 \text{ nm}$.

3. Results

3.1. Characterization

Figure 1 illustrates XRD patterns of ZnFe_2O_4 and different $\text{ZnNd}_x\text{Fe}_{2-x}\text{O}_4$ ($x = 0.01, 0.03, 0.05$) samples synthesized at 500°C . The formation of zinc ferrite (JCPDS number 022-1012) was evidenced by reflection peaks corresponding to the characteristic spacing between (220), (311), (400), (422), (511) and (440) planes of a cubic spinel structure. Employing Scherrer's equation, average crystallite size of the samples could be calculated as follows:

$$D_{\text{XRD}} = \frac{k\lambda}{\beta \cos \theta} \quad (2)$$

where λ , k , β and θ wavelength of the X-ray (0.1504 nm), the Scherrer's constant ($k = 0.89$), the full width at half maximum observed in radians and the angle of diffraction of the (311) peak with the highest intensity, respectively.

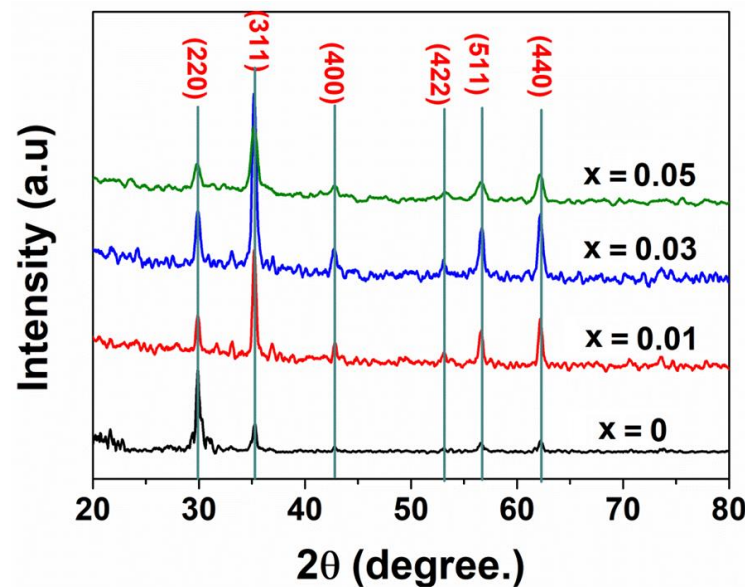


Figure 1. X-ray diffraction patterns of $\text{ZnNd}_x\text{Fe}_{2-x}\text{O}_4$ nanoparticles ($x = 0.0-0.05$) annealed at 500°C .

To determine the lattice constant (a) at the most intense peak (311), following formula was used

$$a = d_{\text{hkl}} \sqrt{h^2 + k^2 + l^2} \quad (3)$$

where d is interplanar distance and h, k, l are Miller indices. The change in crystalline structure with doping of Nd^{3+} ions could be observed from the XRD data given in Table 1. It clearly indicates that the average crystallite sizes significantly decrease from 22 nm to 12 nm with increasing the content of Nd^{3+} from 0 to 0.05 mol , which was in good agreement with a previous publication [36]. Moreover, the lattice constants for the samples of zinc ferrites nanoparticles increase slightly from 8.43 to 8.45 \AA as the amount of Nd^{3+} added increases. This outcome can be due to the difference of the radius of ferrites, or more specifically, metal ions radius ($\text{Nd}^{3+}, \text{Zn}^{2+}, \text{Fe}^{3+}$). Indeed, the ionic radius of Nd^{3+} ion (0.98 \AA) is larger than the ionic radius of Zn^{2+} (0.74 \AA) and Fe^{3+} (0.67 \AA); hence Nd^{3+} ions prefer to occupy more octahedral sites (B-sites) than Fe^{3+} ions [36]. It is likely for Nd^{3+} ions to be distributed in the grain boundaries, thus contributing to the improvement of energy barrier of Zn^{2+} or Fe^{3+} movement [38]. As a result, the growth of ferrites nanoparticles grains and the crystallite size of zinc ferrites tends to decrease while their crystal lattice constant increases. The same phenomena in decreasing crystallite size due to increasing

rare-earth ions content have been observed previously in cobalt ferrites [38,39], nickel ferrites [37] and zinc ferrites [36]. To sum up, the dope of Nd^{3+} showed a significant effect on the crystalline nanostructure of origin zinc ferrites.

Table 1. Average crystallite size (D_{XRD}), lattice parameter (a), unit cell volume (V) and wave number, ν_1 and ν_2 for the tetrahedral and octahedral of the $\text{ZnNd}_x\text{Fe}_{2-x}\text{O}_4$ samples, respectively.

Samples	D_{XRD} (nm)	a (Å)	V (Å ³)	ν_1 (cm ⁻¹)	ν_2 (cm ⁻¹)
ZnFe_2O_4	22	8.43	599.08	522.7	447.5
$\text{ZnNd}_{0.01}\text{Fe}_{1.99}\text{O}_4$	21	8.44	601.21	528.5	451.3
$\text{ZnNd}_{0.03}\text{Fe}_{1.97}\text{O}_4$	18	8.45	603.35	526.0	418.5
$\text{ZnNd}_{0.05}\text{Fe}_{1.95}\text{O}_4$	12	8.45	603.35	526.6	420.5

Chemical bonds diagnosed from the FT-IR spectra in Figure 2 can suggest two most characteristic bands for the as-synthesized $\text{ZnNd}_x\text{Fe}_{2-x}\text{O}_4$ nanoparticles. The first band is located at 522.7–528.6 cm⁻¹ (Table 1), which corresponds to the stretching vibration in the tetrahedral bonding of Zn–O [26,37]. The other band appeared at 418.5–451.3 cm⁻¹, which is attributable to the stretching frequency of the octahedral bonding of Fe–O and Nd–O. The change in the lattice parameters can reflect the shift of the band vibrations. The position and intensity of ν_1 and ν_2 tend to change with increasing Nd^{3+} ions content. Finally, the frequency change confirms the presence of the Nd^{3+} ions occupying the octahedral sites in the ferrites lattice.

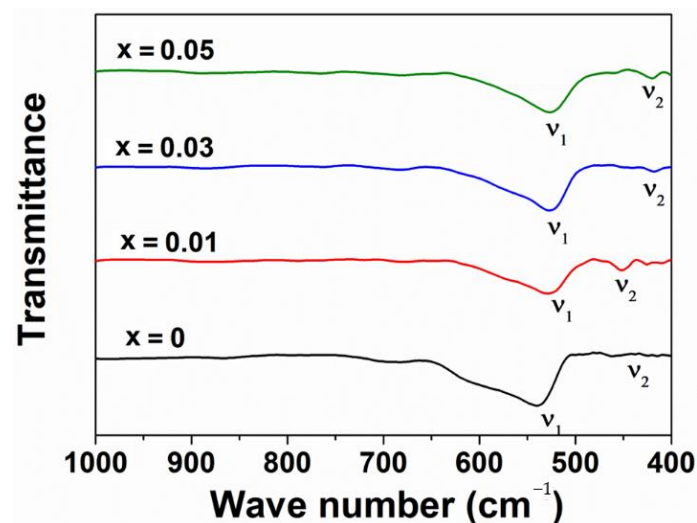


Figure 2. FT-IR spectrum of $\text{ZnNd}_x\text{Fe}_{2-x}\text{O}_4$ nanoparticles.

To better understand the structure of samples, the morphology of $\text{ZnNd}_x\text{Fe}_{2-x}\text{O}_4$ nanoparticles is observed by SEM technique. The samples including pure ZnFe_2O_4 and synthesized $\text{ZnNd}_x\text{Fe}_{2-x}\text{O}_4$ nanoparticles ($x = 0.01$; 0.03 and 0.05) all display a type of uniform sphere (Figure 3). The crystallite size of the zinc ferrites decreases with increasing Nd content, which is consistent with the result of XRD analysis.

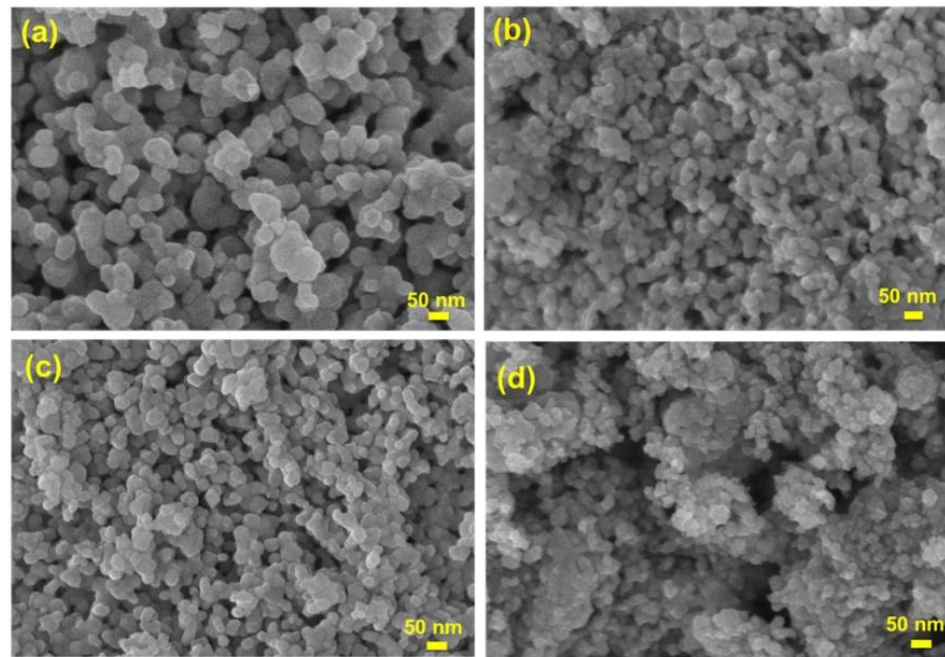


Figure 3. SEM photomicrography of $\text{ZnNd}_x\text{Fe}_{2-x}\text{O}_4$ nanoparticles: (a) $x = 0$, (b) $x = 0.01$, (c) $x = 0.03$, (d) $x = 0.05$.

Figure 4 displays the TEM photomicrography of the pure ZnFe_2O_4 and $\text{ZnNd}_{0.03}\text{Fe}_{1.97}\text{O}_4$ annealed at 500 °C. Both samples $\text{ZnNd}_{0.03}\text{Fe}_{1.97}\text{O}_4$ and ZnFe_2O_4 exhibit mostly homogeneous microspheres. In particular, the agglomeration or clustering of these microspheres is rarely observed. Although the effect of Nd^{3+} ions on the morphology is almost inconsiderable, the particle size of $\text{ZnNd}_{0.03}\text{Fe}_{1.97}\text{O}_4$ sample is smaller than that of the ZnFe_2O_4 sample. The grain size from TEM studied is in close agreement with the XRD data and SEM photomicrography. Moreover, the chemical composition of samples was confirmed by EDX spectra. The presence of all elements in the XRD profile indicates that synthesized material was of high purity (Figure 5).

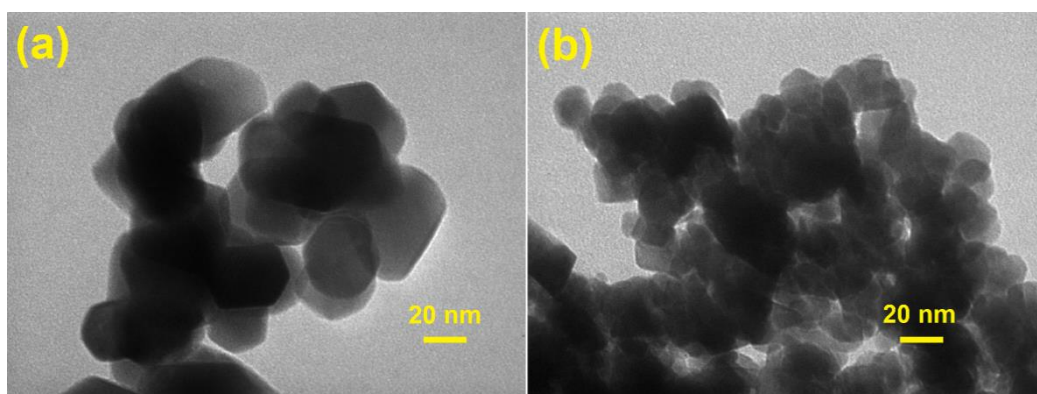


Figure 4. TEM of $\text{ZnNd}_x\text{Fe}_{2-x}\text{O}_4$ nanoparticles: (a) $x = 0$; (b) $x = 0.03$.

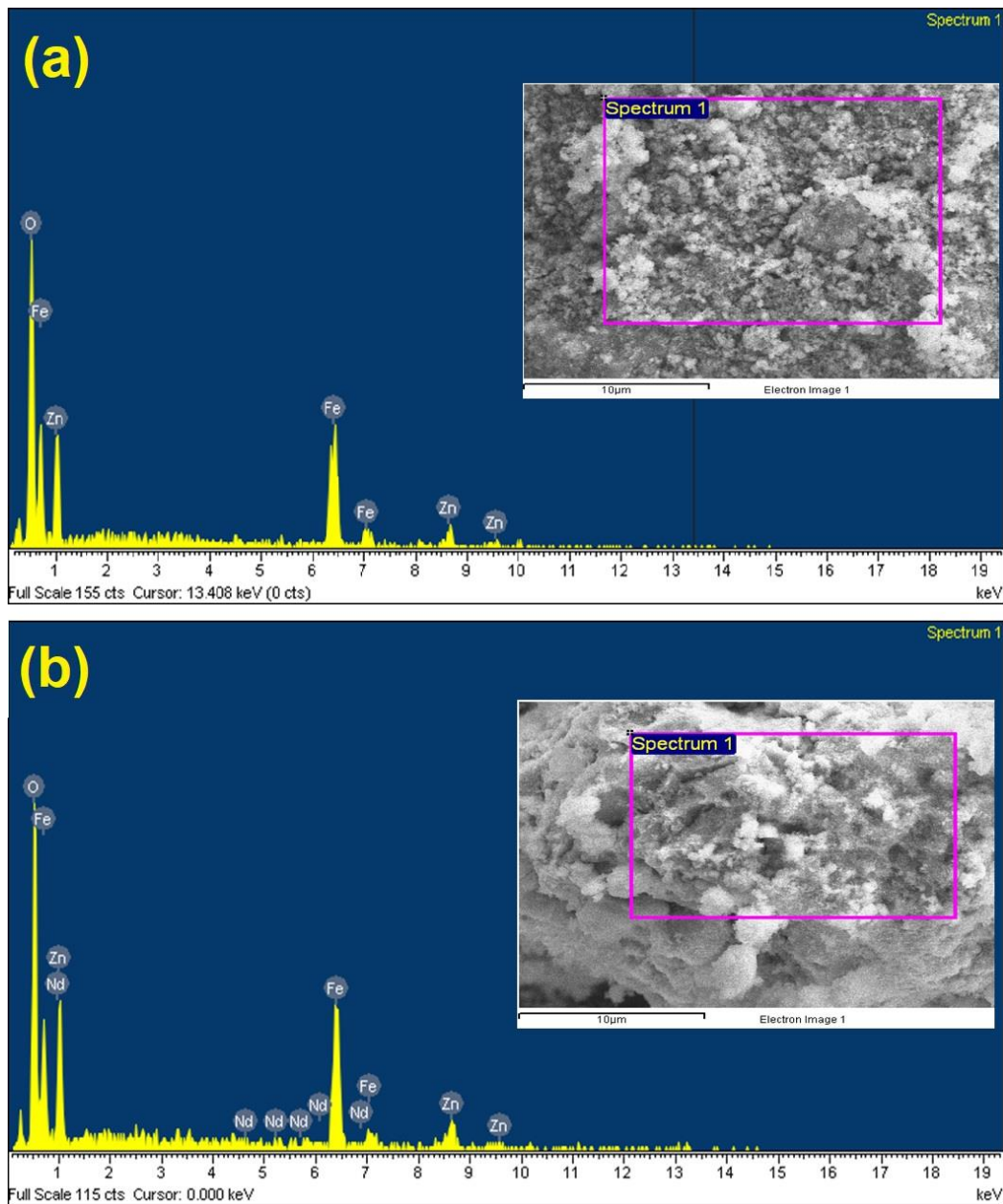


Figure 5. EDX spectra of $\text{ZnNd}_x\text{Fe}_{2-x}\text{O}_4$ nanoparticles: (a) $x = 0$; (b) $x = 0.03$.

The band gap of the spinel nanoparticles was determined by DRS. Kubelka-Munk model was used to calculate band gaps (E_g) of zinc ferrites nanoparticles with the absorption coefficient (α) obtainable from DRS spectra as Equation (4).

$$F(R) = \alpha = \frac{(1 - R)^2}{2R} \quad (4)$$

where, $F(R)$ represents the Kubelka-Munk function, α is the absorption coefficient and R is the reflectance. The following relationship could be used to determine the band gap energy (E_g) as shown in Equation (5).

$$\alpha h\nu = A(h\nu - E_g)^n \quad (5)$$

where, $h\nu$: energy of the photon, α : the the absorption coefficient, A : material parameter and n : transition parameter, $n = 2$ represent indirect transitions. The slope of plotting $(\alpha h\nu)^2$ against $h\nu$ could be used to measure the band gap energy for the absorption peak,

as shown in Figure 6. The band gap values of $\text{ZnNd}_x\text{Fe}_{2-x}\text{O}_4$ ($x = 0, 0.01, 0.03, 0.05$) nanoparticles are found to be 1.75, 1.57, 1.50 and 1.42 eV, respectively. This indicates that the Nd^{3+} ions concentration affected the band gap energy of zinc ferrites nanoparticles. The band gap energy value decreased with increasing the Nd^{3+} ions concentration. Due to the larger ionic radius, the crystal lattice is bound to distort leading to generation of interface defects [38]. In zinc ferrites nanoparticles, the orbital overlapping between O-2p and Fe-3d energy levels caused the formation of the energy band gap. There is the 4f Fermi energy level of Nd in $\text{ZnNd}_x\text{Fe}_{2-x}\text{O}_4$ samples, thus resulting in decreased band gap energy value [42,43]. The optical band gap of the CoFe_2O_4 samples doped with La decreases from 1.35 to 1.1 eV [38].

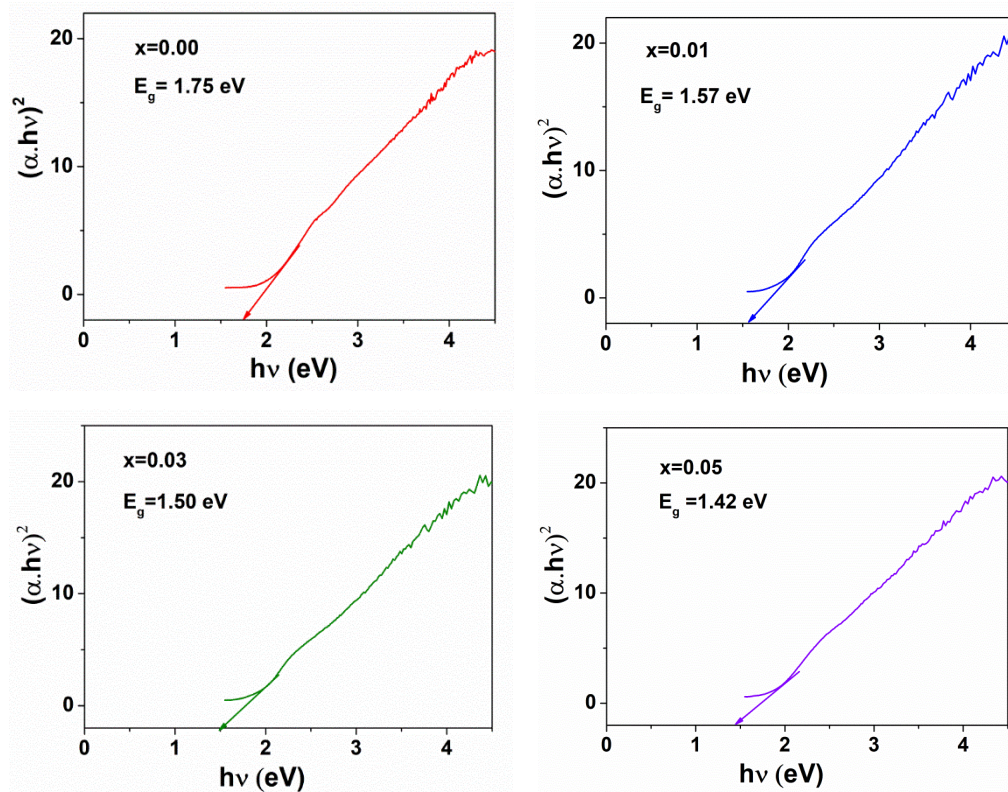


Figure 6. The band gap energies of $\text{ZnNd}_x\text{Fe}_{2-x}\text{O}_4$ nanoparticles ($x = 0.00$ – 0.05).

3.2. Photocatalytic Activity

3.2.1. Influence of Experimental Conditions

The photo-Fenton catalytic degradation activities of ZnFe_2O_4 catalyst occurring at different experimental parameters are illustrated in Figure 7. The lowest RhB removal efficiency is 13.87%, reached only when there is only H_2O_2 existed in the solution. Under ZnFe_2O_4 /Visible-light system, the decolorization ratio achieved 25.35%. This figure was enhanced to 31.51% when ZnFe_2O_4 combined with H_2O_2 . However, the removal rate of RhB reaches to 85.14% under irradiation and in the presence of ZnFe_2O_4 and H_2O_2 . The high removal rate could be explained by the h^+ in the valence of ZnFe_2O_4 and photodecomposition of H_2O_2 that produce more $\bullet\text{OH}$. Both of which contributed to the improved oxidation of dyes [22]. On the other hand, the production of $\bullet\text{OH}$ could also be promoted by decreased recombination of electrons and holes, caused by the participation of photo-induced electrons in the $\text{Fe}^{3+}/\text{Fe}^{2+}$ cycle reaction [26].

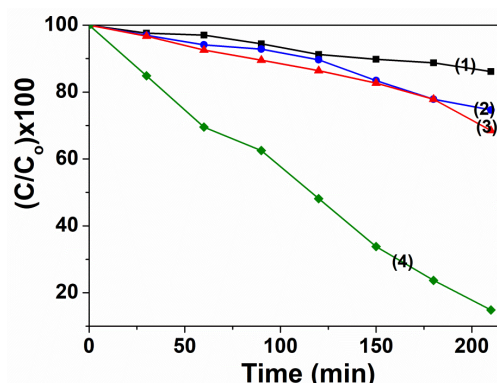


Figure 7. The photocatalytic degradation of RhB in different conditions: curve (1), 10.0 mg/L RhB + 0.04 M H₂O₂ + light; curve (2), 10.0 mg/L RhB + 0.1 g ZnFe₂O₄ + light; curve (3), 10.0 mg/L RhB + 0.1 g ZnFe₂O₄+ 0.04 M H₂O₂ + dark; curve (4), 10.0 mg/L RhB + 0.1 g ZnFe₂O₄ + 0.04 M H₂O₂ + light.

When the ZnFe₂O₄ crystals are doped with Nd³⁺ ions, their photocatalytic degradation of RhB are enhanced. The higher photocatalytic performance at higher Nd³⁺ introduced may be due to smaller crystallite sizes from 22 to 12 nm with increasing Nd³⁺ ions content. This may be leading to the larger surface area and higher amount of active photocatalytic sites. Moreover, another effect is band gap energy value decreasing from 1.75 to 1.42 eV with increasing Nd³⁺ ions concentration, which aids the formation of ·OH active species and stimulates oxidative degradation of dye molecules. UV–vis absorption spectra of RhB during the degradation by ZnNd_xFe_{2–x}O₄ (x = 0–0.05) at the different irradiation time as shown in Figure 8. The photocatalytic degradation efficiency of RhB and kinetic constant after 210 min irradiation are 96.53% and 0.0095 min^{–1}, 98.00% and 0.0189 min^{–1}, 95.46% and 0.0163 min^{–1} in the presence of H₂O₂ and ZnNd_xFe_{2–x}O₄ with x = 0.01, 0.03 and 0.05, respectively (Figure 9 and Table 2). This phenomenon can rely on the combination of rare earth ions and the ions in the crystal lattice of ferrite to generate the energy levels and the defects, which has been confirmed by XRD and DRS measurements [38,39].

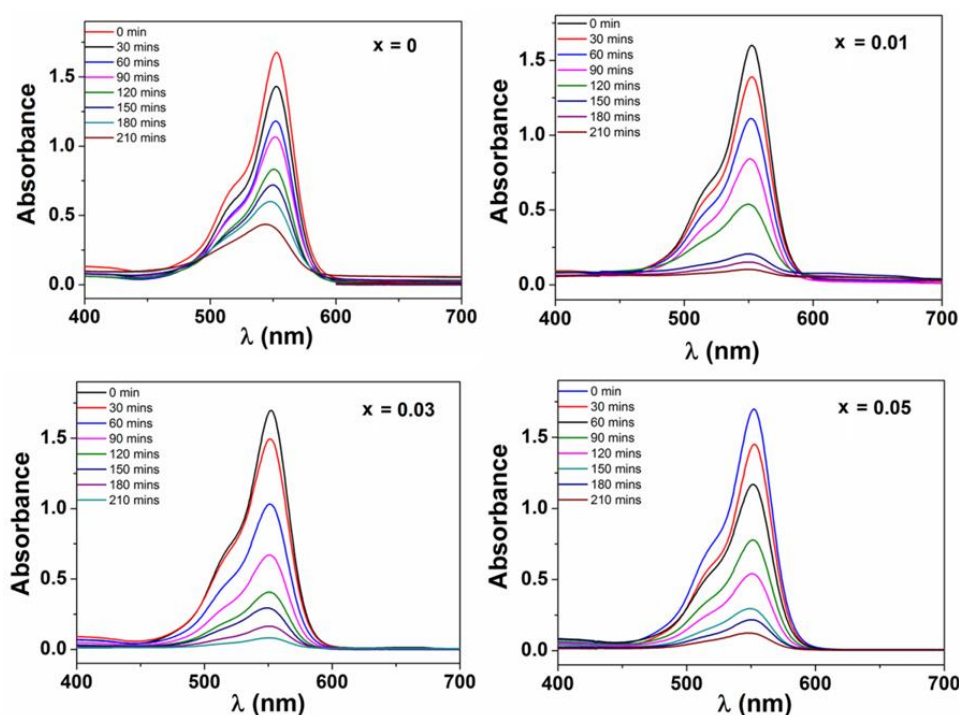


Figure 8. The change in absorption of Rhodamine B solution with time in the presence of H₂O₂ and ZnNd_xFe_{2–x}O₄ nanoparticles (x = 0–0.05) under irradiation.

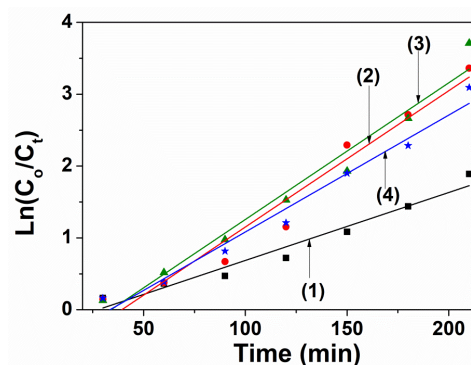


Figure 9. The plots of $\ln(C_0/C_t)$ versus irradiation time (t) in the presence of H_2O_2 and $ZnNd_xFe_{2-x}O_4$ nanoparticles: (1) $x = 0$, (2) $x = 0.01$, (3) $x = 0.03$, (4) $x = 0.05$.

Table 2. The degradation efficiency (H%) and pseudo first-order rate constant (k) for the photocatalytic degradation of RhB in the presence of H_2O_2 0.04 M using $ZnNd_xFe_{2-x}O_4$ nanoparticles.

Samples	H (%)	k (min^{-1})	R^2
$ZnFe_2O_4$	85.14 ± 0.99	0.0095	0.952
$ZnNd_{0.01}Fe_{1.99}O_4$	96.53 ± 0.95	0.0189	0.951
$ZnNd_{0.03}Fe_{1.97}O_4$	98.00 ± 0.44	0.0190	0.964
$ZnNd_{0.05}Fe_{1.95}O_4$	95.46 ± 0.91	0.0163	0.972

3.2.2. Influence of H_2O_2 Concentration

Figure 10 shows the removal efficiency of RhB under different concentrations of H_2O_2 . When initial H_2O_2 concentration increased from 0.02 M to 0.04 M, the degradation efficiency increased from 79.4% to 97.42%. However, the degradation efficiency decreased to 93.02% when H_2O_2 concentration increased to 0.06 M. The initial increase in the degradation could be explained due to the generation of the higher number of $\bullet OH$ active species which are mainly responsible for the oxidative degradation of dye molecules, Equation (3). When hydrogen peroxide presents in high concentration, $\bullet OH$ could be scavenged (Equations (4)–(6)) and reduced [22,26]. Therefore, the degradation efficiency of RhB dye is greatly reduced. The optimal initial H_2O_2 content was 0.04 M.

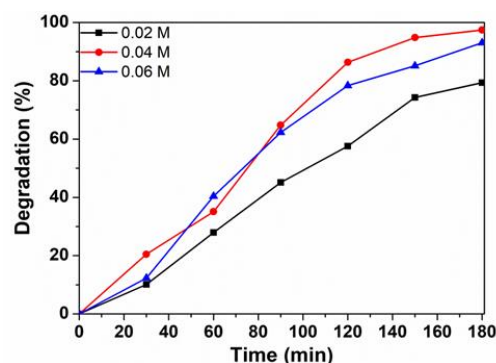


Figure 10. The influence of H_2O_2 concentration on the efficient degradation of Rhodamine B using $ZnNd_{0.03}Fe_{1.97}O_4$ as Photo-Fenton.

3.2.3. Influence of the Catalyst Loading

The effect of the ferrite sample amount on the RhB removal rate is shown in Figure 11. When the $\text{ZnNd}_{0.03}\text{Fe}_{1.97}\text{O}_4$ dosage increases from 0.5 g/L to 0.75 g/L, the efficient degradation of RhB increases from 62.13% to 98.01% at 180 min. However, the removal rate of RhB decreased to 93.02% when increasing the $\text{ZnNd}_{0.03}\text{Fe}_{1.97}\text{O}_4$ dosage to 1.0 g/L. This outcome is because when increasing catalyst dosage, $\bullet\text{OH}$ radical amount increases due to the reaction of h^+ in the valence of ferrite sample [22]. However, with a high catalyst dosage, the degradation efficiency of RhB dye decreases due to increased solution turbidity, in turn obstructing light irradiation and activating the totality of the catalyst suspension [43]. Therefore, the optimal catalyst dosage was 0.75 g/L.

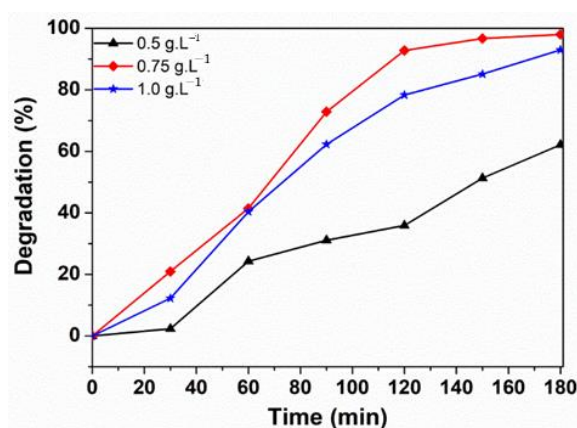


Figure 11. The effect of $\text{ZnNd}_{0.03}\text{Fe}_{1.97}\text{O}_4$ dosage on the degradation of Rhodamine.

4. Conclusions

Nd^{3+} substituted zinc ferrite nanoparticles were successfully synthesized via solution combustion technique. The physical and chemical characteristic of the $\text{ZnNd}_x\text{Fe}_{2-x}\text{O}_4$ samples were investigated by XRD, EDX, FT-IR, SEM and TEM. The average crystallite size and the optical band gap values reduced from 22 to 12 nm and from 1.75 to 1.42 eV, respectively, with increasing Nd^{3+} ions content. The substitution of Nd^{3+} ions on octahedral sites was confirmed by the change of ν_1 and ν_2 frequency. The enhanced photocatalytic activity of the zinc ferrite samples was observed with increasing Nd^{3+} ions concentration. The $\text{ZnNd}_{0.03}\text{Fe}_{1.97}\text{O}_4$ nanoparticles have the highest efficient degradation for Rhodamine B. The removal efficiency of Rhodamine B dye was affected by the concentration of H_2O_2 , catalyst amount. The optimal initial H_2O_2 content was 0.04 M and the optimal dosage of the catalyst was 0.75 g/L.

Author Contributions: Conceptualization, L.T.T.N.; methodology, H.T.T.N.; software, T.H.L.; validation, L.T.H.N.; formal analysis, H.Q.N.; investigation, L.T.T.N.; software, T.T.H.P.; resources, N.D.B.; data curation, N.T.K.T.; writing—review and editing, D.T.C.N.; writing—original draft preparation, L.T.T.N.; writing—review and editing, T.V.L.; visualization, T.V.L.; supervision, T.V.L., T.V.T.; project administration, T.V.T.; funding acquisition, T.V.T. All authors have read and agreed to the published version of the manuscript.

Funding: This work was supported by Thai Nguyen University of Education of Vietnam (No. CS2020-02).

Institutional Review Board Statement: Not applicable.

Informed Consent Statement: Not applicable.

Data Availability Statement: The data presented in this study are available on request from the corresponding author.

Conflicts of Interest: The authors declare no conflict of interest.

References

1. Van Tran, T.; Phan, T.-Q.T.; Nguyen, D.T.C.; Nguyen, T.T.; Nguyen, D.H.; Vo, D.-V.N.; Bach, L.G.; Nguyen, T.D. Recyclable Fe₃O₄@C nanocomposite as potential adsorbent for a wide range of organic dyes and simulated hospital effluents. *Environ. Technol. Innov.* **2020**, *20*, 101122. [[CrossRef](#)]
2. Nguyen, D.T.C.; Dang, H.H.; Vo, D.-V.N.; Bach, L.G.; Nguyen, T.D.; Van Tran, T. Biogenic synthesis of MgO nanoparticles from different extracts (flower, bark, leaf) of *Tecoma stans* (L.) and their utilization in selected organic dyes treatment. *J. Hazard. Mater.* **2021**, *404*, 124146. [[CrossRef](#)]
3. Van Tran, T.; Nguyen, H.-T.T.; Dang, H.H.; Nguyen, D.T.C.; Nguyen, D.H.; Van Pham, T.; Van Tan, L. Central composite design for optimizing the organic dyes remediation utilizing novel graphene oxide@CoFe₂O₄ nanocomposite. *Surf. Interfaces* **2020**, *21*, 100687. [[CrossRef](#)]
4. Hsiao, P.-H.; Li, T.-C.; Chen, C.-Y. ZnO/Cu₂O/Si Nanowire Arrays as Ternary Heterostructure-Based Photocatalysts with Enhanced Photodegradation Performances. *Nanoscale Res. Lett.* **2019**, *14*, 244. [[CrossRef](#)] [[PubMed](#)]
5. Hsiao, P.-H.; Timjan, S.; Kuo, K.-Y.; Juan, J.-C.; Chen, C.-Y. Optical Management of CQD/AgNP@SiNW Arrays with Highly Efficient Capability of Dye Degradation. *Catalysts* **2021**, *11*, 399. [[CrossRef](#)]
6. Khalid, N.R.; Ahmed, E.; Niaz, N.A.; Nabi, G.; Ahmad, M.; Tahir, M.B.; Rafique, M.; Rizwan, M.; Khan, Y. Highly visible light responsive metal loaded N/TiO₂ nanoparticles for photocatalytic conversion of CO₂ into methane. *Ceram. Int.* **2017**, *43*, 6771–6777. [[CrossRef](#)]
7. Khalid, N.R.; Majid, A.; Tahir, M.B.; Niaz, N.A.; Khalid, S. Carbonaceous-TiO₂ nanomaterials for photocatalytic degradation of pollutants: A review. *Ceram. Int.* **2017**, *43*, 14552–14571. [[CrossRef](#)]
8. Khalid, N.R.; Liaqat, M.; Tahir, M.B.; Nabi, G.; Iqbal, T.; Niaz, N.A. The role of graphene and europium on TiO₂ performance for photocatalytic hydrogen evolution. *Ceram. Int.* **2018**, *44*, 546–549. [[CrossRef](#)]
9. Tahir, M.B.; Nabi, G.; Hassan, A.; Iqbal, T.; Kiran, H.; Majid, A. Morphology tailored synthesis of C-WO₃ nanostructures and its photocatalytic application. *J. Inorg. Organomet. Polym. Mater.* **2018**, *28*, 738–745. [[CrossRef](#)]
10. Tahir, M.B.; Nabi, G.; Iqbal, T.; Sagir, M.; Rafique, M. Role of MoSe₂ on nanostructures WO₃-CNT performance for photocatalytic hydrogen evolution. *Ceram. Int.* **2018**, *44*, 6686–6690. [[CrossRef](#)]
11. Tahir, M.; Nabi, G.; Rafique, M.; Khalid, N. Nanostructured-based WO photocatalysts: Recent development, activity enhancement, perspectives and applications for wastewater treatment. *Int. J. Environ. Sci. Technol.* **2017**, *14*, 2519–2542. [[CrossRef](#)]
12. Tahir, M.B.; Nabi, G.; Khalid, N.R. Enhanced photocatalytic performance of visible-light active graphene-WO₃ nanostructures for hydrogen production. *Mater. Sci. Semicond. Process.* **2018**, *84*, 36–41. [[CrossRef](#)]
13. Tahir, M.B.; Nabi, G.; Khalid, N.R.; Rafique, M. Role of europium on WO₃ performance under visible-light for photocatalytic activity. *Ceram. Int.* **2018**, *44*, 5705–5709. [[CrossRef](#)]
14. Tahir, M.B.; Iqbal, T.; Kiran, H.; Hasan, A. Insighting role of reduced graphene oxide in BiVO₄ nanoparticles for improved photocatalytic hydrogen evolution and dyes degradation. *Int. J. Energy Res.* **2019**, *43*, 2410–2417. [[CrossRef](#)]
15. Nguyen, T.D.; Nguyen, V.-H.; Nanda, S.; Vo, D.-V.N.; Nguyen, V.H.; Van Tran, T.; Nong, L.X.; Nguyen, T.T.; Bach, L.-G.; Abdullah, B. BiVO₄ photocatalysis design and applications to oxygen production and degradation of organic compounds: A review. *Environ. Chem. Lett.* **2020**, *18*, 1779–1801. [[CrossRef](#)]
16. Casbeer, E.; Sharma, V.K.; Li, X.-Z. Synthesis and photocatalytic activity of ferrites under visible light: A review. *Sep. Purif. Technol.* **2012**, *87*, 1–14. [[CrossRef](#)]
17. Guo, X.; Wang, D. Photo-Fenton degradation of methylene blue by synergistic action of oxalic acid and hydrogen peroxide with NiFe₂O₄ hollow nanospheres catalyst. *J. Environ. Chem. Eng.* **2019**, *7*, 102814. [[CrossRef](#)]
18. Feng, J.; Zhang, Z.; Gao, M.; Gu, M.; Wang, J.; Zeng, W.; Lv, Y.; Ren, Y.; Fan, Z. Effect of the solvents on the photocatalytic properties of ZnFe₂O₄ fabricated by solvothermal method. *Mater. Chem. Phys.* **2019**, *223*, 758–761. [[CrossRef](#)]
19. Zhao, Y.; Lin, C.; Bi, H.; Liu, Y.; Yan, Q. Magnetically separable CuFe₂O₄/AgBr composite photocatalysts: Preparation, characterization, photocatalytic activity and photocatalytic mechanism under visible light. *Appl. Surf. Sci.* **2017**, *392*, 701–707. [[CrossRef](#)]
20. Vinosha, P.A.; Xavier, B.; Anceila, D.; Das, S.J. Nanocrystalline ferrite (MFe₂O₄, M = Ni, Cu, Mn and Sr) photocatalysts synthesized by homogeneous Co-precipitation technique. *Optik* **2018**, *157*, 441–448. [[CrossRef](#)]
21. To Loan, N.T.; Hien Lan, N.T.; Thuy Hang, N.T.; Quang Hai, N.; Tu Anh, D.T.; Thi Hau, V.; Van Tan, L.; Van Tran, T. CoFe₂O₄ nanomaterials: Effect of annealing temperature on characterization, magnetic, photocatalytic, and photo-Fenton properties. *Processes* **2019**, *7*, 885. [[CrossRef](#)]
22. Cai, C.; Zhang, Z.; Liu, J.; Shan, N.; Zhang, H.; Dionysiou, D.D. Visible light-assisted heterogeneous Fenton with ZnFe₂O₄ for the degradation of Orange II in water. *Appl. Catal. B Environ.* **2016**, *182*, 456–468. [[CrossRef](#)]
23. Xiang, Y.; Huang, Y.; Xiao, B.; Wu, X.; Zhang, G. Magnetic yolk-shell structure of ZnFe₂O₄ nanoparticles for enhanced visible light photo-Fenton degradation towards antibiotics and mechanism study. *Appl. Surf. Sci.* **2020**, *513*, 145820. [[CrossRef](#)]
24. Li, Y.; Chen, D.; Fan, S.; Yang, T. Enhanced visible light assisted Fenton-like degradation of dye via metal-doped zinc ferrite nanosphere prepared from metal-rich industrial wastewater. *J. Taiwan Inst. Chem. Eng.* **2019**, *96*, 185–192. [[CrossRef](#)]
25. Cao, Z.; Zhang, J.; Zhou, J.; Ruan, X.; Chen, D.; Liu, J.; Liu, Q.; Qian, G. Electroplating sludge derived zinc-ferrite catalyst for the efficient photo-Fenton degradation of dye. *J. Environ. Manag.* **2017**, *193*, 146–153. [[CrossRef](#)]

26. Surendra, B.S.; Shekhar, T.R.S.; Veerabhadraswamy, M.; Nagaswarupa, H.P.; Prashantha, S.C.; Geethanjali, G.C.; Likitha, C. Probe sonication synthesis of ZnFe_2O_4 NPs for the photocatalytic degradation of dyes and effect of treated wastewater on growth of plants. *Chem. Phys. Lett.* **2020**, *745*, 137286. [[CrossRef](#)]
27. Mohamed, R.M.; Ismail, A.A. Impact of surfactant ratios on mesostructured MnFe_2O_4 nanocomposites and their photocatalytic performance. *Ceram. Int.* **2020**, *46*, 10925–10933. [[CrossRef](#)]
28. Kalam, A.; Al-Sehemi, A.G.; Assiri, M.; Du, G.; Ahmad, T.; Ahmad, I.; Pannipara, M. Modified solvothermal synthesis of cobalt ferrite (CoFe_2O_4) magnetic nanoparticles photocatalysts for degradation of methylene blue with H_2O_2 /visible light. *Results Phys.* **2018**, *8*, 1046–1053. [[CrossRef](#)]
29. Kefeni, K.K.; Mamba, B.B. Photocatalytic application of spinel ferrite nanoparticles and nanocomposites in wastewater treatment. *Sustain. Mater. Technol.* **2020**, *23*, e00140. [[CrossRef](#)]
30. Nadumane, A.; Shetty, K.; Anantharaju, K.S.; Nagaswarupa, H.P.; Rangappa, D.; Vidya, Y.S.; Nagabhushana, H.; Prashantha, S.C. Sunlight photocatalytic performance of Mg-doped nickel ferrite synthesized by a green sol-gel route. *J. Sci. Adv. Mater. Devices* **2019**, *4*, 89–100. [[CrossRef](#)]
31. Bhukal, S.; Bansal, S.; Singhal, S. Magnetic Mn substituted cobalt zinc ferrite systems: Structural, electrical and magnetic properties and their role in photo-catalytic degradation of methyl orange azo dye. *Phys. B Condens. Matter* **2014**, *445*, 48–55. [[CrossRef](#)]
32. Abraham, A.G.; Manikandan, A.; Manikandan, E.; Vadivel, S.; Jaganathan, S.K.; Baykal, A.; Renganathan, P.S. Enhanced magneto-optical and photo-catalytic properties of transition metal cobalt (Co^{2+} ions) doped spinel MgFe_2O_4 ferrite nanocomposites. *J. Magn. Magn. Mater.* **2018**, *452*, 380–388. [[CrossRef](#)]
33. Sharma, R.; Singhal, S. Structural, magnetic and electrical properties of zinc doped nickel ferrite and their application in photocatalytic degradation of methylene blue. *Phys. B Condens. Matter* **2013**, *414*, 83–90. [[CrossRef](#)]
34. Joshi, S.; Kumar, M.; Pandey, H.; Singh, M.; Pal, P. Structural, magnetic and dielectric properties of Gd_3^+ substituted NiFe_2O_4 nanoparticles. *J. Alloys Compd.* **2018**, *768*, 287–297. [[CrossRef](#)]
35. Chauhan, L.; Singh, N.; Dhar, A.; Kumar, H.; Kumar, S.; Sreenivas, K. Structural and electrical properties of Dy_3^+ substituted NiFe_2O_4 ceramics prepared from powders derived by combustion method. *Ceram. Int.* **2017**, *43*, 8378–8390. [[CrossRef](#)]
36. Zhang, Y.; Chen, Y.; Kou, Q.; Wang, Z.; Han, D.; Sun, Y.; Yang, J.; Liu, Y.; Yang, L. Effects of Nd concentration on structural and magnetic properties of ZnFe_2O_4 nanoparticles. *J. Mater. Sci. Mater. Electron.* **2018**, *29*, 3665–3671. [[CrossRef](#)]
37. Masoudpanah, S.M.; Ebrahimi, S.A.S.; Derakhshani, M.; Mirkazemi, S.M. Structure and magnetic properties of La substituted ZnFe_2O_4 nanoparticles synthesized by sol-gel autocombustion method. *J. Magn. Magn. Mater.* **2014**, *370*, 122–126. [[CrossRef](#)]
38. Mariosi, F.R.; Venturini, J.; da Cas Viegas, A.; Bergmann, C.P. Lanthanum-doped spinel cobalt ferrite (CoFe_2O_4) nanoparticles for environmental applications. *Ceram. Int.* **2020**, *46*, 2772–2779. [[CrossRef](#)]
39. Almessiere, M.A.; Slimani, Y. Sonochemical synthesis of Eu_3^+ substituted CoFe_2O_4 nanoparticles and their structural, optical and magnetic properties. *Ultrason. Sonochem.* **2019**, *58*, 104621. [[CrossRef](#)] [[PubMed](#)]
40. Sharma, R.; Bansal, S.; Singhal, S. Augmenting the catalytic activity of CoFe_2O_4 by substituting rare earth cations into the spinel structure. *RSC Adv.* **2016**, *6*, 71676–71691. [[CrossRef](#)]
41. Rashmi, S.K.; Naik, H.S.B.; Jayadevappa, H.; Sudhamani, C.N.; Patil, S.B.; Naik, M.M. Influence of Sm_3^+ ions on structural, optical and solar light driven photocatalytic activity of spinel MnFe_2O_4 nanoparticles. *J. Solid State Chem.* **2017**, *255*, 178–192. [[CrossRef](#)]
42. Patil, S.B.; Naik, H.S.B.; Nagaraju, G.; Viswanath, R.; Rashmi, S.K. Synthesis of visible light active Gd_3^+ -substituted ZnFe_2O_4 nanoparticles for photocatalytic and antibacterial activities. *Eur. Phys. J. Plus* **2017**, *132*, 1–12. [[CrossRef](#)]
43. Harish, K.N.; Bhojya Naik, H.S.; Prashanth Kumar, P.N.; Viswanath, R. Optical and photocatalytic properties of solar light active Nd-substituted Ni ferrite catalysts: For environmental protection. *ACS Sustain. Chem. Eng.* **2013**, *1*, 1143–1153. [[CrossRef](#)]